Ultrahigh Capacity of Monolayer Dumbbell C_4N as a Promising Anode Material for Lithium-Ion Battery

Journal of The Electrochemical Society, 2020 **167** 020538
1945-7111/2020/167(2)/020538/9/$40.00 © 2020 The Electrochemical Society ("ECS"). Published on behalf of ECS by IOP Publishing Limited

Ultrahigh Capacity of Monolayer Dumbbell C_4N as a Promising Anode Material for Lithium-Ion Battery

Chen Yang,[1,2] Xiuying Zhang,[1] Jiachen Ma,[1] Bowen Shi,[1] Han Zhang,[1] Linqiang Xu,[1] Jie Yang,[1] Shiqi Liu,[1] Ruge Quhe,[3] Feng Pan,[4] Jing Lu,[1,2,5,z] and Dapeng Yu[1,2,6]

[1]*State Key Laboratory for Mesoscopic Physics and Department of Physics, Peking University, Beijing 100871, People's Republic of China*
[2]*Academy for Advanced Interdisciplinary Studies, Peking University, Beijing 100871, People's Republic of China*
[3]*State Key Laboratory of Information Photonics and Optical Communications and School of Science, Beijing University of Posts and Telecommunications, Beijing 100876, People's Republic of China*
[4]*School of Advanced Materials, Peking University, Shenzhen Graduate School, Shenzhen 518055, People's Republic of China*
[5]*Beijing Key Laboratory for Magnetoelectric Materials and Devices, Beijing 100871, People's Republic of China*
[6]*Shenzhen Key Laboratory of Quantum Science and Engineering, Shenzhen 518055, People's Republic of China*

2D carbon nitride materials play an important role in energy storage. Recently, 2D dumbbell (DB) C_4N, a new member of 2D carbon nitride, is proposed and possesses two stable phases (DB C_4N-I and DB C_4N-II). In this paper, we use the first-principles calculations to examine the performance of monolayer (ML) DB C_4N as anode for lithium-ion batteries (LIBs). After adsorbing Li-ions, the Fermi level of both two phases of ML DB C_4N moves upward into the conduction band and shows an enhancement of the electrical conductivity. The maximum theoretical specific capacities for LIBs are up to 1942 and 2158 mAh g^{-1} for I and II phase, respectively, which are about 4 ∼5 times higher than that of the commercially used graphite (372 mAh g^{-1}). The appropriate open-circuit voltages of ∼0.60 and 0.68 V are also generated in ML DB C_4N-I and II anodes, respectively. Finally, the diffusion barriers of Li ions are only 0.26 and 0.21 eV at I and II phase of ML DB C_4N, respectively, providing appropriate rate capacities performance for LIBs. Therefore, we suggest that both two phases of ML DB C_4N are promising anode materials for LIBs.
 [DOI: 10.1149/1945-7111/ab6bbd]

Manuscript submitted November 4, 2019; revised manuscript received December 28, 2019. Published January 29, 2020.

Supplementary material for this article is available online

As one of the most important batteries, rechargeable lithium-ion batteries (LIBs) have attracted more and more attention and achieved great commercial success.[1–5] However, the most extensively and commercially used anode material for LIBs is still graphite, whose specific capacity is only 372 mAh g^{-1}.[6] With the development of electronic devices, it is more and more urgent to strengthen the performance of LIBs, especially the specific capacity. Two-dimensional (2D) materials possess a high surface area, fast ion transport and vast ion occupation. These properties make 2D materials promising electrodes for LIBs that possess a higher specific capacity and larger rate.[7–10]

So far, many kinds of 2D materials have been explored as anodes for LIBs and show a high specific capacity. For instance, graphene has been commercially used for its experimental high specific capacity (540 mAh g^{-1}), stability and low cost.[11] Some 2D transition metal chalcogenides (TMDs) have been investigated and show a high specific capacity like 466 mAh g^{-1} for VS_2 (in theory)[12] and 814.2 mAh g^{-1} for MoS_2 (in the experiment).[13] Previous theoretical studies also show that monolayer (ML) 2D silicene,[14] borophene,[15,16] and black phosphorene[17,18] can generate a high specific capacity of 1196, 1720 and 2596 mAh g^{-1}, respectively. Remarkably, 2D carbon nitride materials often get a tremendous specific capacity as well as good cycling stability both experimentally and theoretically. For instance, 2D C_2N anode possesses a high specific capacity of 933.2 mAh g^{-1} in experiment,[2] and the theoretical specific capacity is up to 2939 mAh g^{-1} for its monolayer.[19] 2D C_3N anode possesses a specific capacity of 383.3 mAh g^{-1} and an excellent cycling stability for more than 500 cycles in the experiment.[2] ML 2D carbon excess C_3N is also predicted to possess a high theoretical specific capacity of 837.06 mAh g^{-1}.[20] In addition, 2D g-C_3N_4 has drawn growing attention for its highly reversible specific capacity of 2753 mAh g^{-1} and high cycling stability (more than 300 cycles) in experiment.[21]

Another important member of 2D carbon nitride is dumbbell (DB) C_4N.[22] After been proposed in 2017, it has initiated a series of studies in theory for its potential applications.[22–25] 2D DB C_4N is predicted to possess two stable DB-shape phases with both thermal and dynamical stability and could be experimentally synthesized as 2D C_3N.[2,22] Besides, the DB-shape structures can probably generate an appropriate diffusion pathway for Li-ions.[26] The Dirac-cone energy band has been found in both two phases of DB C_4N, which means a good electric property.[27] These novel characters of DB C_4N are significant in applications of energy storage. Motivated by the huge success of other 2D carbon nitride materials used as an anode for LIBs, based on the first-principles calculations, we investigate the performance of the ML DB C_4N as an anode material for LIBs.

In this paper, we show that both two phases of ML DB C_4N can adsorb Li atom steadily. After Li-adsorption, the Fermi level of ML DB C_4N moves upward into the conduction band and enhances the electrical conductivity for LIBs. The maximum theoretical specific capacity for LIBs is up to 1942 and 2158 mAh g^{-1} for I and II phase of ML DB C_4N, respectively. As anode for LIBs, ML DB C_4N also possesses appropriate open-circuit voltages of ∼0.60 and 0.68 V for I and II phase, respectively. Besides, we demonstrate the diffusion barriers of Li-ion are only 0.26 and 0.21 eV at I and II phase of ML DB C_4N, respectively. Such low diffusion barriers provide appropriate rate capacities for LIBs. Therefore, we suggest that both two phases of ML DB C_4N are promising anode materials for LIBs with ultrahigh specific capacities, appropriate electrical conductivity, open-circuit voltage, and rate capacity.

Computational Details

All the calculations were carried out by the plane-wave basis set with a cut-off energy of 500 eV and the projector augmented wave (PAW) pseudopotential was implemented in the Vienna ab initio simulation package (VASP) code.[28,29] Based on the density functional theory (DFT), the generalized gradient approximation (GGA) combined with the Perdew-Burke-Ernzerhof (PBE) form were adopted.[30–33] Periodic boundary conditions were implemented in all directions with a vacuum space (at least 15 Å) in the *z*-direction

[z]E-mail: jinglu@pku.edu.cn

between the adjacent ML DB C_4N layers to avoid the interactions in the adjacent unit cells. Herein, we adopted the dipole correction to eliminate the pseudo interaction generated by the periodic boundary condition in the vacuum direction. Besides, Van der Waals interaction was taken into consideration by using the DFT-D3 approach in the VASP code.[34,35]

We firstly optimized the structures of the Li-adsorbed ML DB C_4N compounds by relaxing the atoms and lattice parameters into their energy and force minimization. Herein, the *k*-point mesh was sampled by the Monkhorst–Pack method with a separation of 0.04 $Å^{-1}$ and the convergence thresholds were 10^{-4} eV for energy and 0.02 eV $Å^{-1}$ for force. After the full convergence of the structure optimization, we changed a more precise *k*-point mesh with a separation of 0.02 $Å^{-1}$ and the convergence threshold to 10^{-6} eV for energy. These parameters were used to calculate the total energies and electronic properties (like the partial density of state (PDOS), the charge density difference and the electron localization functions) of the compounds. We also used the Bader charge analysis to estimate the charge distribution situations.[36] Besides, the climbing image nudged elastic band (CI-NEB) method implemented in the VASP transition state tools was used to determine the minimum energy diffusion pathways and the corresponding energy profiles of Li ions.[37,38]

Results and Discussions

Adsorption ability of one Li atom at ML DB C_4N.—ML DB C_4N has been proposed to possess two stable phases named ML DB C_4N-I and ML DB C_4N-II, as shown in Figs. 1a and 1b, respectively.[22] The optimized lattice parameters are $a = b =$ 4.775 Å for phase I and 4.761 Å for phase II, in accord with the reported values.[22] To begin with, the favorable adsorption sites should be found. For ML DB C_4N-I, as shown in Fig. 1a, we define four potential adsorption sites according to its symmetry: the "central sites" above the center of the C–N hexagon (H_1 site) and the C–C hexagon (H_2 site), the "top sites" on the top of the N atom (T_1 site) and the C atom (T_2 site). Both N-surface and C-surface (as defined in Fig. 1) of ML DB C_4N-I are considered in our calculation, as shown in Fig. 1a, which means there are 8 potential adsorption sites for Li atom in total. For ML DB C_4N-II, as shown in Fig. 1b, we define six potential adsorption sites according to its symmetry. The meanings of these adsorption sites in ML DB C_4N-II are similar to those in ML DB C_4N-I.

We simulate a 3 × 3 Ml DB C_4N supercell with one Li atom located above (Li concentration: $Li_{0.05}C_4N$) to investigate the adsorption properties, and such a supercell is large enough to avoid the interaction between the Li atoms in different supercells. Following the previous work,[13,17,20,21,39–42] the adsorption energy (E_b) is defined as:

$$E_b = \frac{E_{Li_xC_4N} - E_{C_4N} - xE_{Li}}{x} \quad [1]$$

where $E_{Li_xC_4N}$, E_{C_4N}, E_{Li} and x are the total energy of ML DB C_4N (I phase or II phase) adsorbed by the Li atoms, the total energy of pristine ML DB C_4N (the corresponding I phase or II phase), the average energy per Li atom in the metal lithium and the number of Li atoms adsorbed in ML DB C_4N, respectively. Depending on such a definition, E_b should be negative when ML DB C_4N adsorbing the Li atom. Besides, the more negative of E_b (in other words, the larger absolute value of E_b), the more exothermic reaction of the Li atom adsorption at ML DB C_4N.[13,17,20,21,39–42]

Table I summarizes the calculated adsorption energies at the different adsorption sites. For the N-surface of ML DB C_4N-I, the studied Li atoms initially on the T_2 and H_2 sites move to the H_1 site after full optimizations. Besides, E_b is positive at the T_1 site, and the absolute value of E_b is close to 0 eV on the H_1 site (only −0.08 eV). Such optimized results and adsorption energy values mean the absence of the adsorption ability for Li atom at the N-surface of ML DB C_4N-I. Thus, in the subsequent part of this paper, we do not study the adsorption at the N-surface of ML DB C_4N-I any more. For the C-surface of ML DB C_4N-I, the studied Li atoms initially on the T_1, T_2 and H_2 sites move to the H_1 site after full optimizations. Besides, the E_b on the H_1 site is −1.38 eV. As for ML DB C_4N-II, the studied Li atoms initially on the T_1, T_2, T_4 and H_2 sites will move to the H_1 site, and E_b on the H_1 and T_3 sites are −0.93 and −0.77 eV, respectively. Thus, we find the favorite adsorption sites for two phases of ML DB C_4N are both in the H_1 sites. The absolute values of E_b on the H_1 site for both two phases of ML DB C_4N are larger than that of the previous studied typical 2D anode materials for LIBs, such as ML 2D BP (−0.202 eV),[43] ML 2D Sc_2C (−0.31 eV)[44] and ML 2D GaN (−0.46 eV).[45] These higher absolute values of adsorption energy of Li atom at ML DB C_4N probably mean better steady adsorption, a more rapid loading process and more significant potential for Li-storage applications.[2,3]

Electronic property of Li adsorbed ML DB C_4N.—A good electrical conductivity is also an important part for the materials intended to be used as an anode for LIBs. In this section, we study the electronic properties of Li adsorbed ML DB C_4N under the low Li concentration of $Li_{0.05}C_4N$. The partial density of states (PDOS) for both two phases of pristine ML DB C_4N-I and the ML DB C_4N-II with one Li atom adsorbed on the H_1 site are illustrated in Fig. 2. For both two phases of pristine ML DB C_4N, there is a Dirac cone around the Fermi level. Such Dirac cones mean an extremely large Fermi velocity and a good electric property. These properties make the pristine ML DB C_4N ideal materials for electronic devices and are also beneficial to LIBs.[22,25] Besides, the states around the Fermi level are mainly composed of p_z atomic orbitals which are

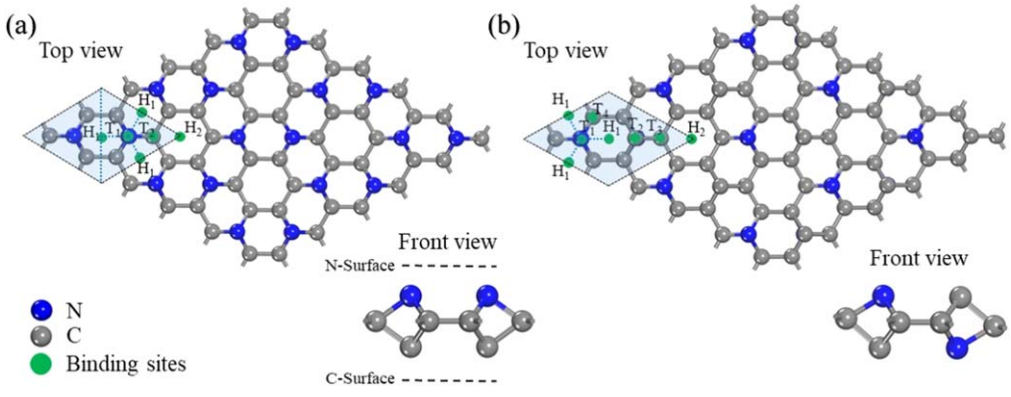

Figure 1. Top and front views of (a) ML DB C_4N-I and (b) ML DB C_4N-II structure. The black dashed lines are the unit cells, and the blue dashed lines help find the symmetry. Herein, we define the "central sites" above the center of the C–N hexagon (H_1 site) and the C–C hexagon (H_2 site), the "top sites" on the top of the N atom (T_1 site) and the C atom (T_2, T_3, and T_4 sites). Both the N-surface and the C-surface of ML DB C_4N-I are considered as marked in its front view figure.

Table I. Adsorption energy of Li atom at different sites in ML DB C_4N-I and ML DB C_4N-II under the concentration of $Li_{0.05}C_4N$. Herein, we define the "central sites" above the center of the C–N hexagon (H_1 site) and the C–C hexagon (H_2 site), the "top sites" on the top of the N atom (T_1 site) and the C atom (T_2, T_3, and T_4 sites). The arrows mean the adsorption site is changed after the optimization.

ML DB C_4N-I N-Surface	Sites	H_1	H_2	T_1	T_2		
	E_b (eV)	−0.08	$\rightarrow H_1$	0.24	$\rightarrow H_1$		
ML DB C_4N-I C-Surface	Sites	H_1	H_2	T_1	T_2		
	E_b (eV)	−1.38	$\rightarrow H_1$	$\rightarrow H_1$	$\rightarrow H_1$		
ML DB C_4N-II	Sites	H_1	H_2	T_1	T_2	T_3	T_4
	E_b (eV)	−0.93	$\rightarrow H_1$	$\rightarrow H_1$	$\rightarrow H_1$	−0.77	$\rightarrow H_1$

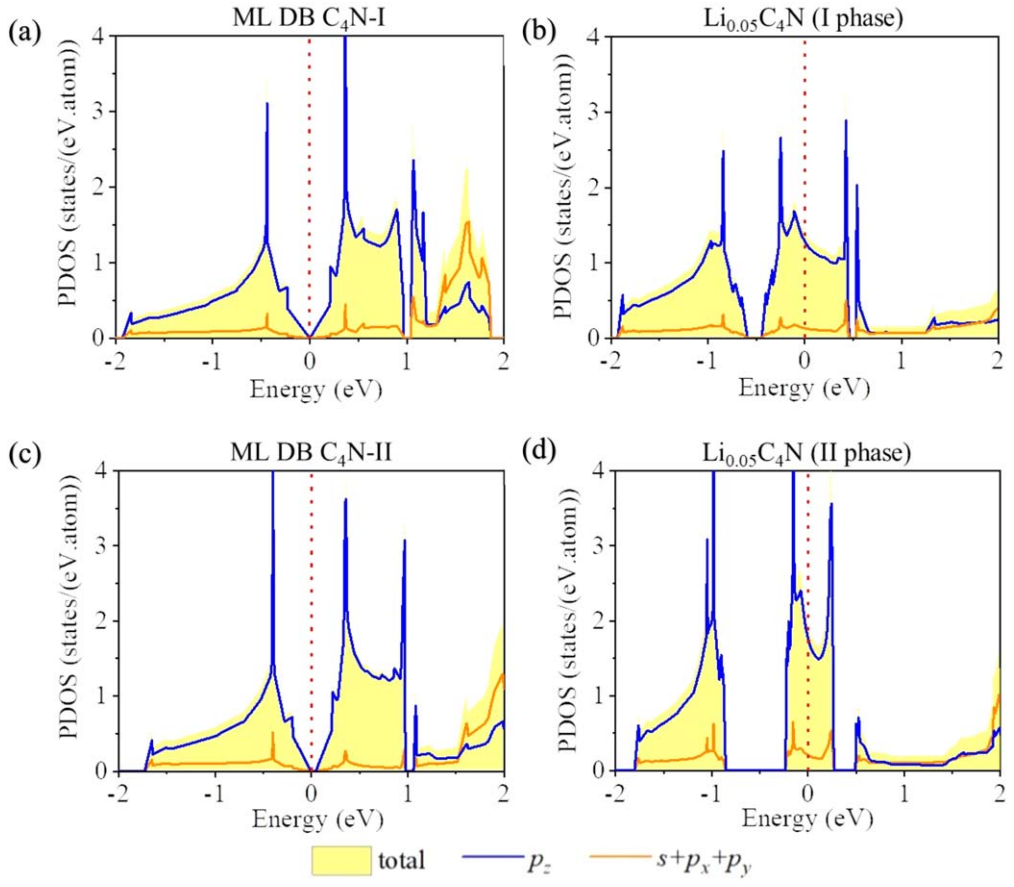

Figure 2. Total density of states and projected density of states (PDOS) of (a) pristine and Li adsorbed ML DB C_4N-I (under the concentration of $Li_{0.05}C_4N$) and (b) pristine and Li adsorbed ML DB C_4N-II (under the concentration of $Li_{0.05}C_4N$). The Fermi level is set to zero.

also the origin of the Dirac cone, in accord with the previous work.[22] As shown in Fig. 2, after the adsorption of the Li atom, the Fermi level of ML DB C_4N moves upward into the conduction band and show an enhancement of the electrical conductivity. Such enhancement will provide a better electrical conductivity in the charge/discharge process for LIBs.

To get a further understanding of the interaction between the Li atom and the two phases of ML DB C_4N, we study the charge transfer of Li-adsorbed ML DB C_4N. The Bader charge analysis indicates that Li atoms act as the electron donors and donate about $0.85e^-$ and $0.87e^-$ per Li atom to the underlying ML DB C_4N-I and II substrates, respectively. Such analyses mean the Li atoms existing in the ionic state after adsorption on the two phases of ML DB C_4N. Besides, the charge density difference ($\Delta\rho$) between the Li atoms and the two phases of ML DB C_4N is also calculated and displayed in Fig. 3 Herein, $\Delta\rho$ is defined as $\Delta\rho = \rho_{LiC_4N} - \rho_{C_4N} - \rho_{Li}$, in which ρ_{LiC_4N}, ρ_{C_4N}, and ρ_{Li} represent the charge density values of the ML DB C_4N adsorbed with the Li-ion, pristine ML DB C_4N, and a Li atom, respectively. As shown in Fig. 3, the red color above the Li atom indicates electron accumulation, and the green color between Li atoms and the ML DB C_4N substrate indicates electron depletion. These charge distributions clearly show a transfer of electrons from the Li atoms to ML DB C_4N for both two phases. Apparently, the adsorbed Li atoms exist in the ionic state. Such ionic states of Li can form a strong Coulomb interaction with ML DB C_4N to enhance the adsorption ability for Li-storage applications. In the following part, we call them Li-ions instead of Li atoms.

Specific capacity of ML DB C_4N for LIBs.—To evaluate the performance of ML DB C_4N as anode for LIBs, the theoretical

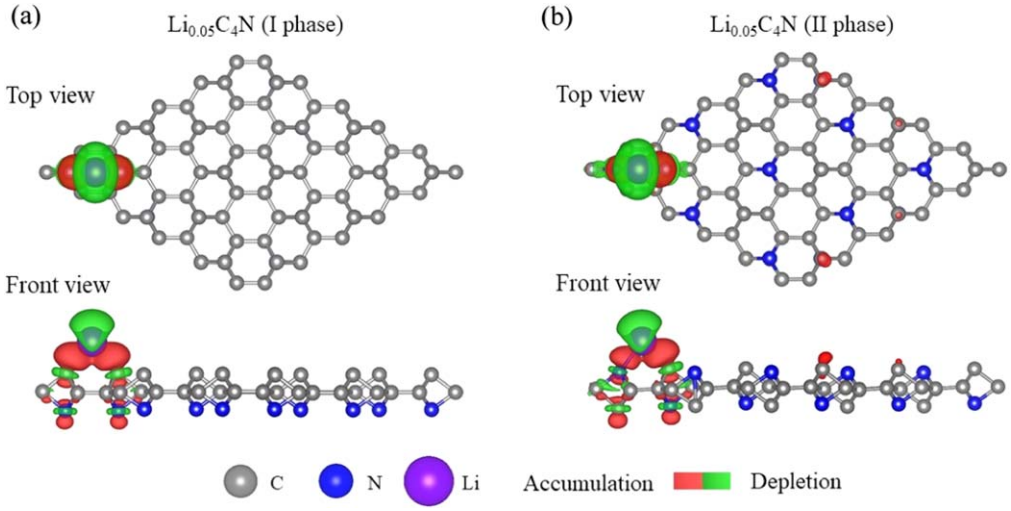

Figure 3. Side and top views of difference charge density for $Li_{0.05}C_4N$ of (a) ML DB C_4N-I and (b) ML DB C_4N-II phases. Red and green colors indicate electron accumulation and depletion, respectively. We adjust the atomic ball radii in terms of the atomic size and mark carbon, nitrogen and lithium atoms in gray, blue and violet colors, respectively.

specific capacity is very important. In theory, the number of the maximum adsorbed Li ions is proportional to the maximum specific capacity of the anode materials for LIBs. Then, we investigate the concentration-dependent adsorption energies of ML DB C_4N. We gradually increase the concentration of Li ions (Li_xC_4N) until the adsorption energy E_b turns to a positive value, and then get the structures with the highest Li concentration ($Li_{x_{max}}C_4N$). Herein, we consider several initial structures of Li_xC_4N with a high highly symmetrical adsorption site for each Li concentration and determine the minimum energy adsorption configuration (Seeing "Method" in Supporting Information for details).[46,47]

For the absence of the adsorption ability for Li-ions at the N-surface of ML DB C_4N-I, only the single-side adsorbing at the C-surface is considered for ML DB C_4N-I. The adsorption energy E_b is negative at low Li concentration, indicating that Li-ML DB C_4N-I compounds are stable. With the increasing Li concentration, the absolute value of E_b becomes smaller due to the weaker electrostatic attraction between the ML DB C_4N-I host and Li cations, as well as the enhanced Li-Li interactions. In the result, E_b keeps negative until $x = 4.5$ for ML DB C_4N-I, as shown in Fig. 4a, and the final structure ($Li_{4.5}C_4N$) is steady, as shown in Fig. 4b.

For ML DB C_4N-II, both two sides can adsorb Li-ions. To begin with, single-side adsorption is considered. Under the similar physical process with ML DB C_4N-I, as a result, E_b keeps negative until $x = 0.5$ for ML DB C_4N-II as shown in Fig. 5a. Besides, the final structure ($Li_{0.5}C_4N$) is steady, as shown in Fig. 5b. However, in the real ML 2D anode, double-side adsorption of Li ions is more possible.[18] Then, we consider the double-side adsorption of Li ions at ML DB C_4N-II. We find that, for any Li concentrations, double-side adsorption is always more stable than that of the single-side, which is attributed to the decrease of Li–Li repulsion in the former case.[18] As shown in Fig. 6a, E_b is negative when $x = 5$ for ML DB C_4N-II, and the structure (Li_5C_4N) is steady, as shown in Fig. 6b. However, when the Li concentration x is increased to 6, the structure (Li_6C_4N) of ML DB C_4N-II anode is broken, as shown in Fig. S1 (available online at stacks.iop.org/JES/167/020538/mmedia). Thus, we consider the maximum Li concentration is $x_{max} = 5$ for the double-side adsorption of ML DB C_4N-II.

We perform the ab initio molecular dynamics (MD) simulation on the ML DB C_4N structures with the highest Li concentration ($Li_{4.5}C_4N$ for I phase and Li_5C_4N for II phase, respectively). The MD simulation is conducted in a canonical NVT ensemble with the 300 K Nose-Hoover thermostat.[48,49] As shown in Fig. S2, the structures of $Li_{4.5}C_4N$ for I phase and Li_5C_4N for II phase are kept during the MD process of up to 2000 fs, suggesting both the systems are thermodynamically stable at 300 K. Thus, we find the ML DB C_4N anodes with the maximum Li storages are $Li_{4.5}C_4N$ for the phase I and Li_5C_4N for the phase II, respectively.

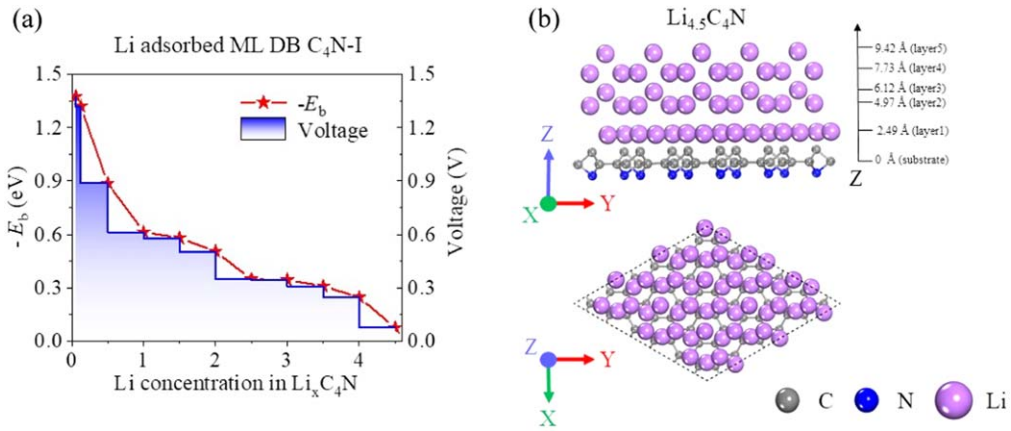

Figure 4. (a) Adsorption energy ($-E_b$) (marked in red) and voltage profiles (marked in blue) as a function of x of Li_xC_4N in ML DB C_4N-I. (b) Front- and top-viewed structure of ML DB C_4N-I with the maximum Li concentration ($Li_{4.5}C_4N$). Herein, we mark the 1st–5th layer of Li ions and their distance to the ML DB C_4N-I surface in the Z-axis. The axis labels (X-Y-Z) are also marked in the figure. We adjust the atomic ball radii in terms of the atomic size and mark carbon, nitrogen and lithium atoms in gray, blue and violet colors, respectively.

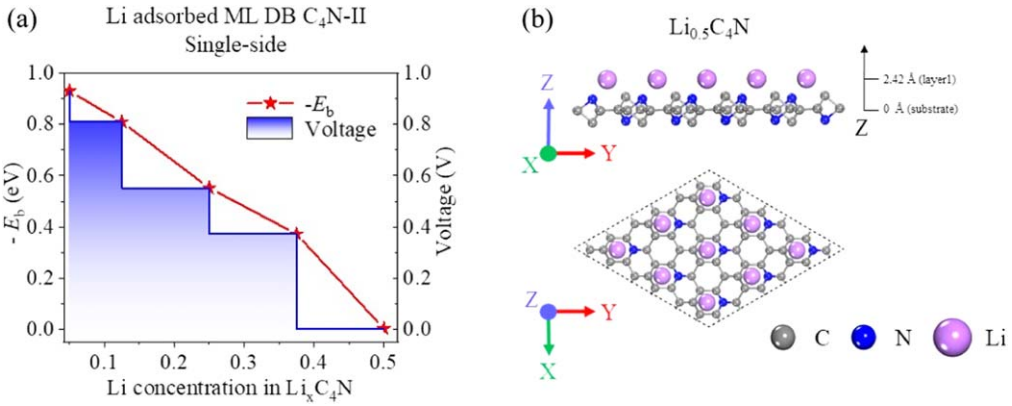

Figure 5. (a) Adsorption energy (-E_b) (marked in red) and voltage profiles (marked in blue) as a function of x of Li_xC_4N in the single-side adsorption condition of ML DB C_4N-II. (b) Front- and top-viewed structure of ML DB C_4N-II with the maximum Li concentration ($Li_{0.5}C_4N$) in the single-side adsorption condition. Herein, we mark the distance of Li ions to the ML DB C_4N-II surface in the Z-axis. The axis labels (X-Y-Z) are also marked in the figure. We adjust the atomic ball radii in terms of the atomic size and mark carbon, nitrogen and lithium atoms in gray, blue and violet colors, respectively.

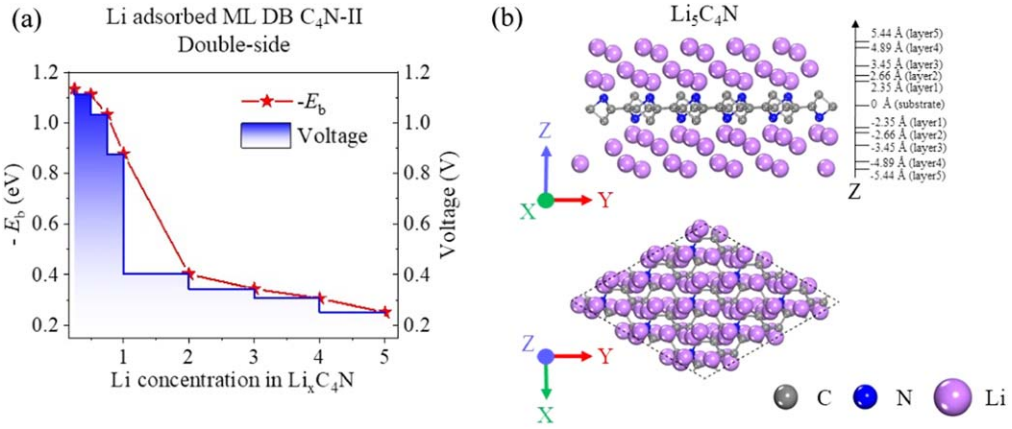

Figure 6. (a) Adsorption energy (-E_b) (marked in red) and voltage profiles (marked in blue) as a function of x of Li_xC_4N in the double-side adsorption condition of ML DB C_4N-II. (b) Front- and top-viewed structure of ML DB C_4N-II with the maximum Li concentration (Li_5C_4N) in the double-side adsorption condition. Herein, we mark the 1st-5th layer of Li ions and their distance to the ML DB C_4N-II surface for double-side in the Z-axis. The axis labels (X-Y-Z) are also marked in the figure. We adjust the atomic ball radii in terms of the atomic size and mark carbon, nitrogen and lithium atoms in gray, blue and violet colors, respectively.

Besides, we calculate the surface normal dipole moment and the total charge transfer with the increase of Li concentration for both I- and II-phase Li-adsorbed ML DB C_4N anode, as shown in Fig. S3. For the I phase, the surface normal dipole moment is increasing gradually with the increase of Li concentration, and the direction of surface normal dipole moment is always from Li atoms to ML DB C_4N-I substrate. However, the total charge transfer keeps around 1.93 e^- per unit-cell from Li atoms to ML DB C_4N-I substrate. Thus, the distance between the centers of positive charges in the Li atoms and negative charges in the ML DB C_4N-I substrate is increasing due to the increase of Li-layer. As for ML DB C_4N-II anode, the total charge transfer keeps around 2.39 e^- per unit-cell from Li-atoms to the underlying ML DB C_4N-II substrate. However, due to the double-side adsorption of Li-atoms (which means the double-side charge transfer) in DB C_4N-II anode, the surface normal dipole moment is self-counteracted and keeps almost zero. These results mean that Li atoms always act as the electron donors and donate steady electrons to the underlying ML DB C_4N anodes in the whole charge process, implying a stable electrochemical performance of ML DB C_4N anodes.[50]

To find the maximum specific capacity (C) of ML DB C_4N, we use the following equation based on the previous work:[13,17,20,21,39–42]

$$C = \frac{1}{M_{C_4N}} \times x_{max} \times F \quad [2]$$

where x_{max} represents the highest concentration of Li ions, F is the Faraday constant (26801 mAh mol^{-1}), M_{C_4N} is the atomic Molar weight of ML DB C_4N (68.039 g mol^{-1}).

The calculated specific capacities are 1942 and 2158 mAh g^{-1} for ML DB C_4N-I and ML DB C_4N-II, respectively. Such ultrahigh specific capacities of both two phases of ML DB C_4N outdistance the commercially used graphite (372 mAh g^{-1}). They are about quadruple of the specific capacities of ML Mn_2N (432 mAh g^{-1}),[40] ML Sc_2C (462 mAh g^{-1})[44] and GaS (526.74 mAh g^{-1}).[46] Besides, they are about double the specific capacities of ML Mn_2C (879 mAh g^{-1}),[40] ML GaN (938 mAh g^{-1}),[51] and ML V_2C (940 mAh g^{-1}).[52] A more detailed comparison of the specific capacities between both two phases of ML DB C_4N and other typical ML 2D anode materials for LIBs is shown in Fig. 7.[6,12,15,16,24,39–42,44,45,53–56]

In addition, the comparison with the other 2D carbon nitride materials as anode for LIBs is also demonstrated in Table II.[2,19–21] It could be concluded that carbon nitride materials usually perform with high specific capacity as anode material for LIBs. Particularly,

Table II. Comparison of the specific capacity of ML DB C4N with the other carbon nitride materials as anode for LIBs.[2,19–21]

2D Carbon Nitride Materials	Capacity (mAh g^{-1})	Exp. or Cal.?	References
Layered 2D C_2N	933.2	Experiment	2
ML C_2N	2939	Calculation	19
Layered 2D C_3N	383.3	Experiment	2
ML Carbon excess C_3N	837.06	Calculation	20
Layered 2D g-C_3N_4	2753	Experiment	21
ML DB C_4N-I phase	1942	Calculation	This work
ML DB C_4N-II phase	2158	Calculation	This work

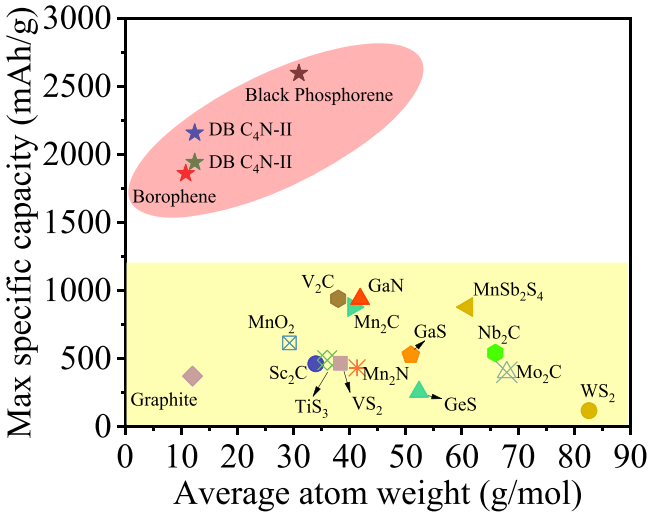

Figure 7. Comparison of the capacities between ML DB C_4N and other typical ML 2D anode materials for LIBs. 3D commercial graphite is also listed for comparison. The data are taken from literature.[6,12,15,16,24,39–42,44,45,53–56]

extremely high specific capacities are generated in ML DB C_4N probably due to two major factors:

(1) The small atomic Molar weight of the carbon and nitrogen elements. Because the specific capacity is defined as a negative correlation with the atomic Molar weight of the anode materials, the anode with a smaller average atom weight could probably more easily generate a higher specific capacity. The average atom weight of ML DB C_4N (13.61 g mol^{-1}) is much lower than those of the previously studied anode like ML Mn_2C (41.24 g mol^{-1}),[40] ML GaS (50.90 g mol^{-1}),[46] and ML WS_2 (82.65 g mol^{-1})[42] and generate a higher specific capacity for LIBs, as shown in Fig. 7.

(2) The existence of multilayer adsorption of Li ions. Usually, with the increasing Li layer, the adsorption ability of the anode would be decreased due to the reduced electrostatic attraction between the anode host and Li cations and the enhanced Li-Li interactions. However, multilayer adsorption of Li ions is observed in ML DB C_4N. Here, electron localization functions (ELFs) are calculated to study such a multilayer adsorption behavior of the ML DB C_4N with the maximum Li concentration, as shown in Fig. 8. For both two phases of ML DB C_4N, we find a large number of localized electrons between the first layer of Li ions and the ML DB C_4N substrate, suggesting an ionic bond character between Li and ML DB C_4N substrate. Such an ionic bond strengthens the adsorption of Li layers. Besides, the repulsion between the two Li layers are neutralized by the electron-cloud filled into the interstices between the two Li layers, and then the adsorption of multilayer Li ions is stabilized. From above, ML DB C_4N anode can get stable multiplayer adsorption of Li ions. Such multilayer adsorption is also found in previous reports like MoO_2/graphene heterostructure anode[47] and ML holey C_2N anode,[19] which results in their relatively high specific capacities for LIBs.

Open-circuit voltage of ML DB C_4N for LIBs.—Open-circuit voltage (OCV) is another factor that needs to be considered for characterizing the performance of LIBs. We can obtain the OCV curve by calculating the average voltage over the increasing values of the Li concentration. In theory, the charge/discharge process can be summarized as:

$$(x_2 - x_1)Li^+ + (x_2 - x_1)e^- + Li_{x_1}C_4N \leftrightarrow Li_{x_2}C_4N \qquad [3]$$

When the pressure, volume and entropy effects are neglected, the average voltage of Li_xC_4N in the concentration range of $x_1 < x < x_2$

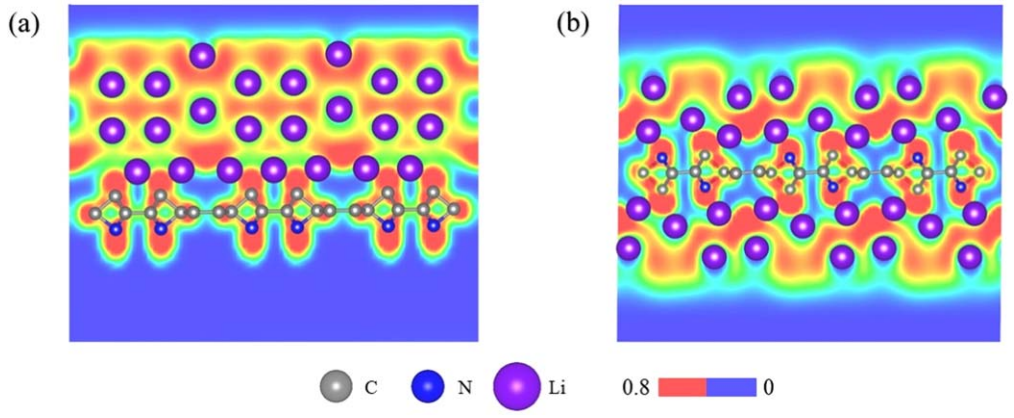

Figure 8. Electron localization functions plots of the (110) slices for (a) ML DB C_4N-I phase and (b) ML DB C_4N-II phase with the highest Li concentration. Red color indicates the localization of valence electrons, and blue means no valence electron here. We adjust the atomic ball radii in terms of the atomic size and mark carbon, nitrogen and lithium atoms in gray, blue and violet colors, respectively.

can be calculated as:[13,17,20,21,39–42]

$$V \approx \frac{E_{Li_{x_1}C_4N} - E_{Li_{x_2}C_4N} + (x_2 - x_1)E_{Li}}{(x_2 - x_1)e} \quad [4]$$

where $E_{Li_{x_1}C_4N}$ and $E_{Li_{x_2}C_4N}$ are the total energy of $Li_{x_1}C_4N$ and $Li_{x_2}C_4N$, E_{Li} is the average energy of per Li atom in the metal lithium, x_1 and x_2 are the number of Li ions adsorbed at the ML DB C_4N surface. In this study, we set $x_1 = 0$ and gradually increase x_2. Thus, Eq. 3 directly simulates each concentration of Li-ions adsorbing at the surface of the ML DB C_4N substrate, which could be simplified as $xLi^+ + xe^- + LiC_4N \leftrightarrow Li_xC_4N$. Under such a particular case, we could also simplify Eq. 4 as $V \approx -\frac{E_b}{e}$ under the same Li-ion concentration.

As shown in Figs. 4a and 6a, the OCV by numerically averaging the voltage profiles are about 0.60 and 0.68 V for ML DB C_4N-I and II anodes, respectively. Usually, a lower OCV of LIBs can guarantee a higher energy density, but a too low OCV for anode would result in metal plating. On the other hand, a too high OCV is not suitable for LIBs because it results in a lower output voltage of the battery. Thus, the suitable OCV for an anode material is suggested in the range of $0.2 \sim 1.0$ V.[57] Fortunately, the OCV of both two phases of ML DB C_4N are just in this range for LIBs. Thus, both two phases of ML DB C_4N possess the appropriate average OCV for LIBs.

Diffusion barriers of the Li-ion at ML DB C_4N.—In the last, we estimate the rate capacity performance of both two phases of ML DB C_4N when used as the anode for LIBs. We have proved that the Li atoms are ionized after adsorbing at the surface of both two phases of ML DB C_4N, and the entities of Li that diffuse at the surface of both two phases of ML DB C_4N should be also Li-ions instead of Li atoms. The migration pathway and barrier of the Li ions diffusion at the surface of both two phases of ML DB C_4N are indispensable to evaluate their rate performance. The diffusion barrier determines the charge/discharge rate of LIBs. We examine the optimal diffusion pathways and calculate the corresponding diffusion barriers by the CI-NEB method in a 3×3 supercell of both two phases of ML DB C_4N. Such a huge supercell has a quite low concentration of Li ions ($Li_{0.05}C_4N$) to avoid the interaction between the Li ions in different supercells.

For ML DB C_4N-I, only the H_1 site at the C-surface can adsorb Li-ion, and the H_2 site is unstable with Li adsorption. Thus, we only consider the diffusion pathway along $H_1 \rightarrow T_2 \rightarrow H_1$. Then, the linear medial diffusion points are inserted along with two nearest neighboring H_1 sites on ML DB C_4N-I. After full optimizations by the CI-NEB method, the inserted medial point gets to their saddle points. The corresponding diffusion energy profiles are presented in Fig. 9a. Herein, the diffusion barrier is 0.26 eV, and the pathway length is about 2.55 Å. For ML DB C_4N-II, considering the symmetry of material, there are two pathways named "B" and "R", as shown in Fig. 9b. Similar to the study of that in ML DB C_4N-I, the diffusion barriers are 0.20 and 0.21 eV, and the corresponding pathway lengths are about 3.26 and 2.63 Å for pathway "B" and "R", respectively. For each Li-ion diffusing at ML DB C_4N-II, both "B" and "R" pathway should be passed. Thus, Li-ion should overcome a diffusion barrier of 0.21 eV at ML DB C_4N-II.

Theoretically, the diffusion barrier is related to the molecular diffusion constant, which can be estimated by the Arrhenius equation:[13,17,20,21,39–42]

$$D \sim \exp\left(\frac{-E}{k_B T}\right) \quad [5]$$

where E is the diffusion barrier, k_B is the Boltzmann's constant and T is the environmental temperature.

The diffusion barriers are only 0.26 and 0.21 eV for Li-ions at I and II phase ML DB C_4N, respectively, which are smaller than those

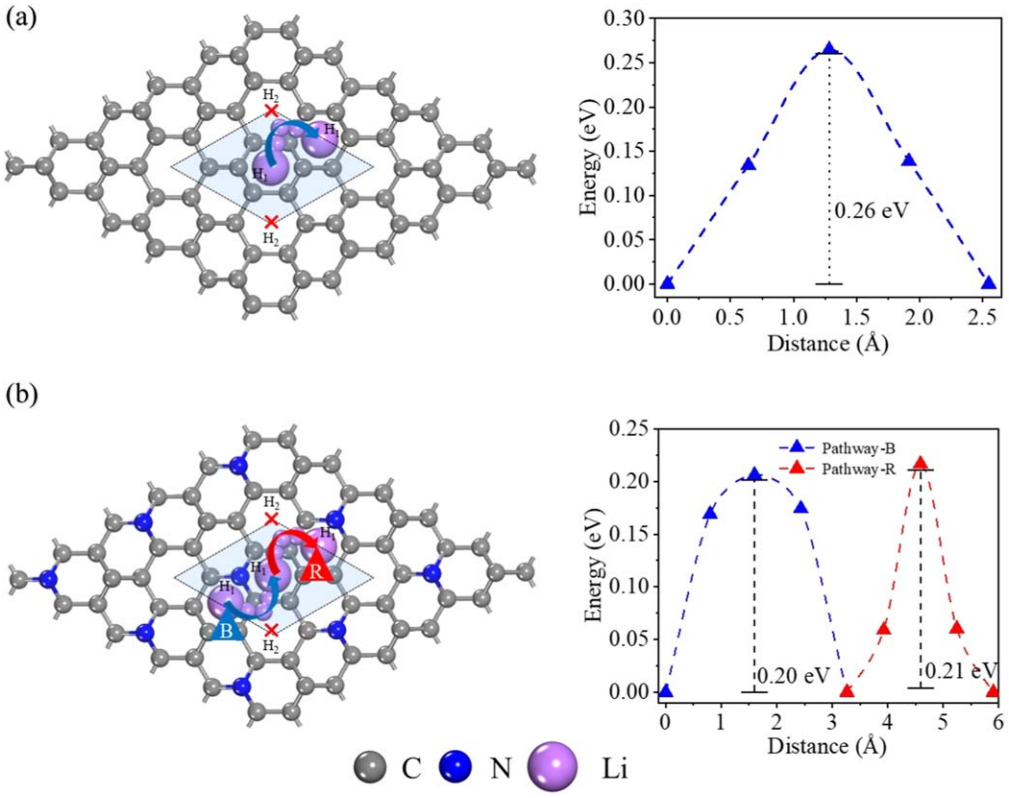

Figure 9. Li atom diffusing pathways and corresponding energy profiles at the surfaces of (a) ML DB C_4N-I and (b) ML DB C_4N-II. The dashed line means the unit-cell of ML DB C_4N. H_2 sites are calculated unstable for Li adsorption, which are marked red "×" in the figure. Curved arrows stand for the diffusing pathways. Red and blue triangles mark the name of the pathway. We adjust the atomic ball radii in terms of the atomic size and mark carbon, nitrogen and lithium atoms in gray, blue and violet colors, respectively.

on the 2D graphene (0.33 eV)[11] as well as the most commercially used bulk graphite (0.48 eV).[6,58] Thus, the diffusion constants of Li ions at both two phases of ML DB C_4N are smaller than those of 2D graphene and bulk graphite. Besides, such low diffusion barriers are as low as those of other anode materials such as ML MoS_2 (0.21 eV)[59] and ML VS_2 (0.22 eV).[12] Therefore, both two phases of ML DB C_4N have appropriate rate capacities performance for LIBs.

Conclusions

In summary, we investigate the performance of ML DB C_4N as the anode material for LIBs by using the first-principles calculations. We firstly show that both the two phases of ML DB C_4N can adsorb Li atom steadily, and the Fermi level of ML DB C_4N will move upward into the conduction band. Thus, both the two phases of ML DB C_4N show an enhancement of the electroconductibility for LIBs. Secondly, the maximum theoretical specific capacity for LIBs is calculated as high as 1942 and 2158 mAh g^{-1} of I and II phase of ML DB C_4N, respectively. Such ultrahigh capacity values outdistance that of the commercially used graphite (372 mAh g^{-1}). Thirdly, as anode for LIBs, ML DB C_4N also possesses appropriate OCV of ∼0.60 and 0.68 V for I and II phase, respectively. Finally, the diffusion barriers of Li-ion are only 0.26 and 0.21 eV at I and II phase of ML DB C_4N, respectively. The low diffusion barriers provide appropriate rate capacities for LIBs. From the above, we conclude that both two phases of ML DB C_4N are promising anode materials for LIBs with ultrahigh specific capacities, appropriate electrical conductivity, open-circuit voltage and rate capacity.

Discussion

In our study, ML DB C_4N is a theoretical material that is predicted based on the ML C_3N framework.[22] Considering the very similar structure between DB C_4N and C_3N, we predict that the interaction of layered 2D DB C_4N anode with the solvent/electrolyte could be also similar to that of layered 2D C_3N anode in the application. Jong-Beom Baek's group has researched the layered 2D C_3N in the experiment as anode for LIBs.[2] After the electrode-electrolyte activation at a low C-rate of 0.1 C in the initial cycle, layered 2D C_3N delivered a reversible capacity of 313.1 mAh g^{-1}, which is higher than that of the graphite anode (80.52 mAh g^{-1}). Excellent cycling stability for more than 500 cycles was also observed in the layered 2D C_3N anode. According to the good performance of C_3N anode interacting with solvent/electrolyte, we predict that the interaction of layered 2D DB C_4N with the solvent/electrolyte could also be stable, and DB C_4N will also possibly keep their high specific capacities in the experiment.

Acknowledgment

This work was supported by the Ministry of Science and Technology of China (No. 2016YFB0700600 (National Materials Genome Project) and 2017YFA206303), the National Natural Science Foundation of China (No. 11674005, 91964101, and 11664026), and by the High-performance Computing Platform of Peking University.

References

1. J. B. Goodenough and K. Youngsik, "Challenges for rechargeable Li batteries." *Chem. Mater.*, **22**, 587 (2010).
2. J. Xu, J. Mahmood, Y. Dou, S. Dou, F. Li, L. Dai, and J. B. Baek, "2D Frameworks of C_2N and C_3N as new anode materials for lithium-ion batteries." *Adv. Mater.*, **29**, 1702007 (2017).
3. U. Alexander, S. Dong-Hwa, and C. Cerbrand, "Computational understanding of Li-ion batteries." *NPJ Comput. Mater.*, **2**, 16010 (2016).
4. L. Shi and T. S. Zhao, "Recent advances in inorganic 2D materials and their applications in lithium and sodium batteries." *J. Mater. Chem. A*, **5**, 3735 (2017).
5. R. Xu, X. Zou, B. Liu, and H. Cheng, "Computational design and property predictions for two-dimensional nanostructures." *Mater. Today*, **21**, 391 (2018).
6. K. Persson, Y. Hinuma, Y. S. Meng, A. V. D. Ven, and G. Ceder, "Thermodynamic and kinetic properties of the li-graphite system from first-principles calculations." *Phys. Rev. B*, **82**, 125416 (2010).
7. G. Fiori, F. Bonaccorso, G. Lannaccone, T. Palacios, D. Neumaier, A. Seabaugh, S. K. Banerjee, and L. Colombo, "Electronics based on two-dimensional materials." *Nat. Nanotechnol.*, **9**, 768 (2014).
8. C. Yang, Y. Luo, J. X. Guo, Y. Pu, D. He, Y. D. Jiang, J. Xu, and Z. J. Liu, "Wideband tunable mid-infrared cross polarization converter using rectangle-shape perforated graphene." *Opt. Express*, **24**, 16913 (2016).
9. L. L. Peng, Y. Zhu, D. H. Chen, R. S. Ruoff, and G. Yu, "Two-dimensional materials for beyond-lithium-ion batteries." *Adv. Energy Mater.*, **6**, 1600025 (2016).
10. J. Liu and X. W. Liu, "Two-dimensional nanoarchitectures for lithium storage." *Adv. Mater.*, **24**, 4097 (2012).
11. E. Yoo, J. Kim, E. Hosono, H. S. Zhou, T. Kudo, and I. Honma, "Large reversible li storage of graphene nanosheet families for use in rechargeable lithium ion batteries." *Nano Lett.*, **8**, 2277 (2008).
12. Y. Jing, Z. Zhou, C. R. Cabrera, and Z. Chen, "Metallic VS_2 monolayer: A promising 2D anode material for lithium ion batteries." *J. Phys. Chem. C*, **117**, 25409 (2013).
13. Y. Lu, X. Yao, J. Yin, G. Peng, P. Cui, and X. Xu, "MoS_2 nanoflowers consisting of nanosheets with a controllable interlayer distance as high-performance lithium ion battery anodes." *RSC Adv.*, **5**, 7938 (2015).
14. S. Xu, X. Fan, J. Liu, D. J. Singh, Q. Jiang, and W. Zheng, "Adsorption of li on single-layer silicene for anodes of li-ion batteries." *Phys. Chem. Chem. Phys.*, **20**, 8887 (2018).
15. H. R. Jiang, Z. H. Lu, M. C. Wu, F. Ciucci, and T. S. Zhao, "Borophene: a promising anode material offering high specific capacity and high rate capability for lithium-ion batteries." *Nano Energy*, **23**, 97 (2016).
16. M. Bohayra, D. Arezoo, R. Obaidur, C. Gianaurelio, and R. Timon, "Borophene as an anode material for Ca, Mg, Na or Li ion storage: a first-principle study." *J. Power Sources*, **329**, 456 (2016).
17. W. Li, Y. Yang, G. Zhang, and Y.-W. Zhang, "Ultrafast and directional diffusion of lithium in phosphorene for high-performance lithium-ion battery." *Nano Lett.*, **15**, 1691 (2015).
18. V. V. Kulish, O. I. Malyi, C. Persson, and P. Wu, "Phosphorene as an anode material for na-ion batteries: a first-principles study." *Phys. Chem. Chem. Phys.*, **17**, 13921 (2015).
19. D. H. Wu, B. C. Yang, H. Y. Chen, and E. Ruckenstein, "Nitrogenated holey graphene C_2N monolayer anodes for lithium- and sodium-ion batteries with high performance." *Energy Storage Mater.*, **16**, 574 (2019).
20. Q. Liu, B. Xiao, J. B. Cheng, Y. C. Li, Q. Z. Li, W. Z. Li, X. F. Xu, and X. F. Yu, "Carbon excess C_3N: a potential candidate as li-ion battery material." *ACS Appl. Mater. Inter.*, **10**, 37135 (2018).
21. J. Chen, Z. Mao, L. Zhang, D. Wang, R. Xu, L. Bie, and B. D. Fahlman, "Nitrogen-deficient graphitic carbon nitride with enhanced performance for lithium ion battery anodes." *ACS Nano*, **11**, 12650 (2017).
22. L. Y. Li, X. R. Kong, O. Leenaerts, X. Chen, B. Sanyal, and F. M. Peeters, "Carbon-rich carbon nitride monolayers with dirac cones: dumbbell C_4N." *Carbon*, **118**, 285 (2017).
23. L. Y. Li, X. R. Kong, and F. M. Peeters, "New nanoporous graphyne monolayer as nodal line semimetal: double dirac points with an ultrahigh fermi velocity." *Carbon*, **141**, 712 (2019).
24. B. Peng, B. Mortazavi, H. Zhang, H. Z. Shao, K. Xu, J. Li, G. Ni, T. Rabczuk, and H. Y. Zhu, "Tuning thermal transport in C_3N monolayers by adding and removing carbon atoms." *Phys. Rev. Appl.*, **10**, 034046 (2018).
25. X. Min, W. Hongyan, S. Songsong, L. Hengtao, L. Xiumei, C. Yuanzheng, and N. Yuxiang, "First-principles study of metal atoms adsorption on two-dimensional dumbbell C_4N." *Phys. Status Solidi b*, **257**, 1900205 (2020).
26. X. Y. Zhang et al., "Absorption and diffusion of lithium on layered InSe." *Computational Condensed Matter.*, **21**, e00404 (2019).
27. X. R. Kong, L. Y. Li, and F. M. Peeters, "Topological dirac semimetal phase in Ge_xSN_y alloys." *Appl. Phys. Lett.*, **112**, 251601 (2018).
28. P. E. Blochl, "Projector augmented-wave method." *Phys. Rev. B*, **50**, 17953 (1994).
29. G. Kresse and D. Joubert, "From ultrasoft pseudopotentials to the projector augmented-wave method." *Phys. Rev. B*, **59**, 1758 (1999).
30. G. Kresse and J. Hafner, "Ab initio molecular dynamics for liquid metals." *Phys. Rev. B*, **47**, 558 (1993).
31. G. Kresse and J. Furthmuller, "Efficient iterative schemes for ab initio total-energy calculations using a plane-wave basis set." *Phys. Rev. B*, **54**, 11169 (1996).
32. G. Kresse and J. Hafner, "Ab initio molecular-dynamics simulation of the liquid-metal–amorphous-semiconductor transition in germanium." *Phys. Rev. B*, **49**, 14251 (1994).
33. J. P. Perdew, K. Burke, and M. Ernzerhof, "Generalized gradient approximation made simple." *Phys. Rev. Lett.*, **78**, 1396 (1997).
34. S. Grimmea, J. Antony, S. Ehrlich, and H. Krieg, "A consistent and accurate ab initio parametrization of density functional dispersion correction (DFT-D) for the 94 elements H-Pu." *J. Chem. Phys.*, **132**, 154104 (2010).
35. S. Grimme, S. Ehrlich, and L. Goerigk, "Effect of the damping function in dispersion corrected density functional theory." *J. Comput. Chem.*, **32**, 1456 (2011).
36. W. Tang, E. Sanville, G. Henkelman, and A. Grid-Based Bader, "Analysis algorithm without lattice bias." *J. Phys. Condens. Matter*, **21**, 084204 (2009).
37. G. Henkelman and H. Jónsson, "Improved tangent estimate in the nudged elastic band method for finding minimum energy paths and saddle points." *J. Chem. Phys.*, **113**, 9978 (2000).
38. G. Henkelman, H. Jónsson, and A. Climbing Image, "Nudged elastic band method for finding saddle points and minimum energy paths." *J. Chem. Phys.*, **113**, 9901 (2000).

39. J. Wu, D. Wang, H. Liu, W. M. Lau, and L. M. Liu, "An ab initio study of TiS_3: a promising electrode material for rechargeable Li and Na ion." *Batteries. RSC Advances*, **5**, 21455 (2015).
40. Y. G. Zhou and X. T. Zu, "Mn_2c sheet as an electrode material for lithium-ion battery: a first-principles prediction." *Electrochim. Acta*, **235**, 167 (2017).
41. Y. Zhang, "First principles prediction of two-dimensional tungsten carbide (W_2C) monolayer and its Li storage capability." *Computational Condensed Matter.*, **10**, 35 (2017).
42. R. Bhandavat, L. David, and G. Singh, "Synthesis of surface-functionalized WS_2 nanosheets and performance as li-ion battery anodes." *J. Phys. Chem. Lett.*, **3**, 1523 (2012).
43. H. R. Jiang, W. Shyy, M. Liu, L. Wei, M. C. Wua, and T. S. Zhao, "Boron phosphide monolayer as a potential anode material for alkali metal-based batteries." *J. Mater. Chem. A*, **5**, 672 (2017).
44. X. Lv, W. Wei, Q. Sun, L. Yu, B. Huang, and Y. Dai, "Sc_2C as a promising anode material with high mobility and capacity: a first-principles study." *ChemPhysChem*, **18**, 1627 (2017).
45. A. Sannyal, Z. Q. Zhang, X. F. Gao, and J. K. Jang, "Two-dimensional sheet of germanium selenide as an anode material for sodium and potassium ion batteries: first-principles simulation study." *Comp. Mater. Sci.*, **154**, 204 (2018).
46. X. Y. Zhang et al., "Monolayer gas with high ion mobility and capacity as a promising anode battery material." *J. Mater. Chem. A*, **7**, 14042 (2019).
47. J. C. Ma, J. Fu, M. Q. Niu, and R. G. Quhe, "Moo_2 and graphene heterostructure as promising flexible anodes for lithium-ion batteries." *Carbon*, 357 (2019).
48. S. A. Nose, "Molecular dynamics method for simulations in the canonical ensemble." *Mol. Phys.*, **52**, 255 (1984).
49. W. G. Hoover, "Canonical dynamics: equilibrium phase-space distributions." *Phys. Rev. A: At. Mol. Opt. Phys.*, **31**, 1695 (1985).
50. J. Su, T. Duan, W. Li, B. Xiao, G. Zhou, Y. Pei, X. Wang, and A. First-Principles, "Study of 2D antimonene electrodes for Li ion storage." *Appl. Surf. Sci.*, **462**, 270 (2018).
51. X. Zhang, L. Jin, X. Dai, G. Chen, and G. Liu, "Two-dimensional GaN: an excellent electrode material providing fast ion diffusion and high storage capacity for Li-Ion and Na-Ion." *Batteries. ACS Appl. Mater. Inter.*, **10**, 38978 (2018).
52. J. Hu, B. Xu, C. Ouyang, S. A. Yang, and Y. Yao, "Investigations on V_2C and V_2CX_2 (X = F, OH) Monolayer as a promising anode material for Li ion batteries from first-principles calculation." *J. Phys. Chem. C*, **118**, 24274 (2014).
53. H. Liu, Y. Du, Y. Deng, and P. D. Ye, "Semiconducting black phosphorus: synthesis, transport properties and electronic applications." *Chem. Soc. Rev.*, **44**, 2732 (2015).
54. S. Deng, L. Wang, T. J. Hou, and Y. Y. Li, "Two-dimensional MnO_2 as a better cathode material for lithium ion batteries." *J. Phys. Chem. C*, **119**, 28783 (2015).
55. Z. Z. Zhang, Y. F. Zhang, Y. Li, J. Lin, D. G. Truhlar, and S. P. Huang, "$MnSb_2S_4$ monolayer as an anode material for metal-ion batteries." *Chem. Mater.*, **30**, 3208 (2018).
56. D. Çakır, C. Sevik, O. Gülseren, and F. M. Peeters, "Mo_2C as a high capacity anode material: a first-principles study." *J. Mater. Chem. A*, **4**, 6029 (2016).
57. C. Eames and M. S. Islam, "Ion intercalation into two-dimensional transition-metal carbides: global screening for new high-capacity battery materials." *J. Am. Chem. Soc.*, **136**, 16270 (2014).
58. K. Toyoura, Y. Koyama, A. Kuwabara, F. Oba, and I. Tanaka, "First-principles approach to chemical diffusion of lithium atoms in a graphite intercalation compound." *Phys. Rev. B*, **78**, 214303 (2008).
59. Y. Li, D. Wu, Z. Zhou, C. R. Cabrera, and Z. Chen, "Enhanced Li adsorption and diffusion on MoS_2 Zigzag nanoribbons by edge effects: a comaputational study." *J. Phys. Chem. Lett.*, **3**, 2221 (2012).